10.2514/6.2023-0451

Simulations of Alternative Propellants for Inductive Pulsed Plasma Thrusters

Tate M. Gill *, Christopher L. Sercel†, and Benjamin A. Jorns‡
University of Michigan, Plasmadyamics and Electric Propulsion Laboratory, Ann Arbor, MI, 48109

A comparison of pure xenon gas to a 1:6 mixture of xenon and carbon dioxide as a propellant for inductive pulsed plasma thrusters is presented. For this comparison, a 5-kW rotating magnetic field thruster was operated on both propellants, and time-resolved internal plasma properties were measured using a triple Langmuir probe. These measurements were used to inform a global plasma chemistry model of these propellants which included the effects of electronic, rotational, and vibrational excitation, dissociation, and recombination. It is found that the xenon case suffered from excitation loss from the production of electronically excited xenon and sustained ionization. An estimate for the plasma efficiency of this case is calculated to be 3.8%. The CO_2 case exhibited low ionization as well as little energy coupling, and electron energy was primarily lost due to the production of CO, O, O+, and CO+. An estimate for the plasma efficiency of this case is calculated to be 9.2%. The limitations of this study are discussed including a path for improving model accuracy.

I. Nomenclature

A	=	thruster surface area
a_{ij}	=	stoichiometric coefficient of species i in reaction j
$E_{loss,i}$	=	energy loss for product i
E_p	=	energy coupled into plasma
e	=	unit charge
ϵ_i	=	enthalpy of formation for product i
η_p	=	effective plasma efficiency
k_j	=	rate for reaction j
m_e	=	electron mass
m_i	=	ion mass
n_e	=	electron density
n_{rj}	=	density of reactant r in reaction j
$P_{diffusion}$	=	total power loss due to thermal diffusion
P_{thrust}	=	thrust power
ϕ	=	sheath potential
S	=	electrode collection area
T_e	=	electron temperature
τ	=	cycle time
V	=	thruster volume
V_{d2}	=	Voltage differential between Langmuir probe electrodes 1 and 2
V_{d3}	=	Voltage differential between Langmuir probe electrodes 1 and 3

II. Introduction

The most well-characterized electric propulsion (EP) technologies such as gridded ion thrusters (GIT) and Hall effect thrusters (HET) are well established in their ability to deliver high specific impulse propulsion and operate for

*Ph.D. Candidate, Department of Aerospace Engineering, University of Michigan, Ann Arbor, MI. AIAA Student Member
†Ph.D. Candidate, Department of Aerospace Engineering, University of Michigan, Ann Arbor, MI. AIAA Student Member
‡Associate Professor, Department of Aerospace Engineering, University of Michigan, Ann Arbor, MI. AIAA Associate Fellow

missions lasting tens of thousands of hours. While well-proven, these devices exhibit a dependence on rare noble gases for propellant. As the demand for higher power EP grows [1], there is an ever-increasing requirement for the propellants to support the ground testing required for long-duration in-space missions. Gases such as xenon and even krypton are becoming increasingly costly to acquire and become prohibitive for the development of high-power variants of traditional EP architectures. An alternative technology suited to address the need for super megawatt electric propulsion is a class of devices known as inductive pulsed plasma thrusters (IPPTs). Generally, IPPTs operate by sequentially discharging large primary coil currents to indirectly induce azimuthal mirror currents within the ionized plasma; these are then driven via the Lorentz force to produce thrust [2]. Because these plasma currents are induced through a time-varying magnetic field, IPPTs do not require the use of plasma-wetted electrodes, thus allowing them to be operated on a wide range of propellants such as organic and inorganic molecules, which can be derived from in-situ resource utilization [3], shared by chemical rockets in dual mode systems [4] or collected from their exhaust byproducts.

Given this advantage, IPPTs have been the subject of several previous research works [5–9]. The most notable result of these efforts was the development of the Pulsed Inductive Thruster (PIT). The principle structure of the PIT consisted of a spiraling planar primary coil and a downstream neutral gas injector. In its most optimized configuration, the PIT exhibited 50% efficiency and 7000 s specific impulse operating on ammonia propellant [3, 10, 11]. However, the PIT suffered from two key challenges. Poor gas confinement due to the planar geometry inherently led to low mass utilization, and high voltages — up to 60 kV to drive the coil currents—posed both an arcing risk and a major challenge for power processing.

The subject of this work, the rotating magnetic field thruster (RMF) is an alternate IPPT technology that aims to address the critical challenges of the PIT thruster. RMF thrusters operate through the use of a magnetic field that spins transversely about the thruster axis. This magnetic field (the RMF) is produced by a series of saddle coils carrying high-frequency AC currents fired with careful offset phasing similar to the operation of an induction motor. The RMF acts as the primary ionization source in addition to entraining the electrons into the azimuthal plasma current which produces thrust. The current produced by an RMF is independent to first order on the magnitude of the primary coil currents which is contrary to conventional IPPTs. The current is instead primarily dependent on the frequency of rotation of the RMF. As a direct result, this change of dependencies eliminates the need for RMF thrusters to operate in the same high voltage regime as their other IPPT counterparts [6, 10, 11]. This reduction in voltage significantly reduces the stress on the driving circuitry which better favors scaling to high powers and duty cycles.

Because of their unique current drive, RMF thrusters are a promising candidate for future high-power IPPT technology, and several research groups have pursued RMF thruster development. Notable contributors include Magnetic Systems North West (MSNW) and the University of Washington, Tokyo University of Agriculture and Technology, and our work at the University of Michigan [12–17]. These studies have demonstrated that RMF thrusters, to date, have exhibited poor efficiency. For example, MSNW indirectly inferred an 8% efficiency with a delivered impulse per shot of 1.0 mN-s for the ELF thruster [18]. More recently, we at the University of Michigan have operated our 5-kW class RMF thruster and directly measured a per-shot impulse efficiency of 0.5% and 400 s specific impulse [9]. The leading explanation for this characteristic inefficiency are large radiative losses caused by high plasma density during operation [19]. Due to their pulsed nature, IPPTs are subject to the buildup of slow and dense neutral gas which is followed by rapid and thorough ionization throughout the volume when inductive power is applied. This causes a peak flash of dense plasma where substantial power (on the order of 50 W or greater) can be radiated away. In support of this claim, both Polzin et al. [3] (PIT) and Weber [18] (ELF) state that large radiative losses, given the high densities inherent to IPPTs, could compose a substantial energy sink. Furthermore, the high efficiency of the PIT thrusters operation on ammonia was attributed to low radiative losses, though the physics was not discussed in detail in that report [11].

In light of these findings, the goal of this work is to assess the suitability of various propellants with a dual purpose. First, to prove out alternative non-noble propellants for inductive thrusters. And second, to identify those propellants which exhibit low collisional losses. We pursue this goal by employing a 0D time-resolved plasma chemistry code which is informed and validated against experimental plasma diagnostic measurements from RMF thruster operation. To this end, this paper is organized in the following way. We begin in Sec. III with a description of the thruster test article, vacuum test facility, and plasma diagnostics employed. We continue in Sec. IV with a description of the plasma chemistry model as well as an overview of relevant performance calculations. We then show in Sec. V the results of our thruster simulations and compare them against the experimental near-field plasma measurements. Lastly, in Sec. VI we discuss the consequences of these results and frame them in the context of future RMF thruster performance.

III. Experimental Setup

In this section, we describe the experimental setup and the diagnostics used to perform the validation measurements which we compare to the simulated results. We first describe the RMF test article and the vacuum facility where it was tested followed by a detailed description of the plasma diagnostics.

A. Test Article and Vacuum Facility

The IPPT used in this experiment is the PEPL RMFv2 thruster, and we show in Figure 1 a photograph of it installed in the test facility. The PEPL RMFv2 is a 5-kW class device that features a two-phase RMF system, a series of three DC electromagnets, and a LaB_6 hollow cathode for seed ionization. The antennas are driven by a 4 kW resonant sin inverter developed by Eagle Harbor Technologies [20] which operates at 415 kHz. Further details on the design of the PEPL RMFv2 thruster are provided by Sercel et al. in Ref. [9].

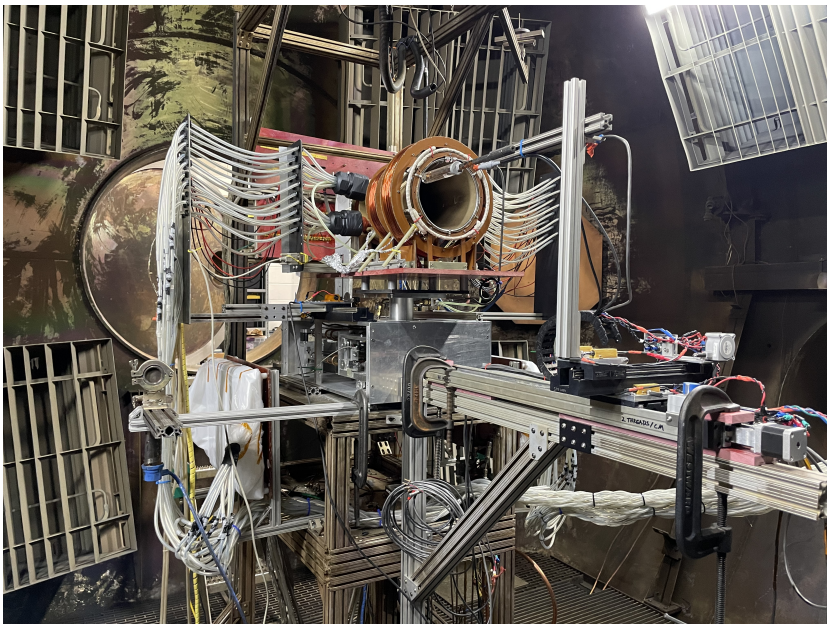

Fig. 1 PEPL RMFv2 thruster installed for testing in the Large Vacuum Test Facility at the University of Michigan.

For this work, the thruster was operated on two different gas mixtures pure xenon and a xenon carbon dioxide mixture. The PEPL RMFv2 thruster hosts both a cathode propellant injector as well as a downstream annular neutral injector. In both cases, the cathode was fed 15 sccm Xe (1.3 mg/s) and the neutral injector was supplied with either 30 sccm Xe or 90 sccm CO_2 maintaining a constant mass flow rate (2.7 mg/s). The remaining operating conditions for the thruster are provided in Table 1.

For testing, we operated the thruster inside the Large Vacuum Test Facility (LVTF) at the University of Michigan. LVTF has a maximum pumping speed of 600 kL/s on Xenon, and during thruster firing the pressures inside the chamber stabilized at 2.9e-6 Torr Xe and 4.4e-6 Torr CO_2 respectively. These pressures were measured using an ion gauge placed at a 1m distance from the thruster centerline coincident with the exit plane of the thruster following best practices for electric propulsion testing [21].

B. Plasma Diagnostic Measurements

To measure the plasma properties within the thruster, we employed a series of three wall-mounted triple Langmuir probes (TLP). Triple Langmuir probes provide an instantaneous measurement of both electron temperature and density by effectively taking three points on the full plasma I-V curve with an assumed Maxwellian plasma. The probe consists of three electrodes, each at a different potential. We allow electrode 2 to electrically float, and we enforce a floating bias voltage on the order of the electron temperature between electrodes 1 and 3, in this case 28 V. The measurements are recorded as the current passing through electrodes 1 and 3, and the voltage differential between electrodes 1 and 2.

Table 1 Standard Operating Conditions for PRPL RMFv2

Parameter	Value
RMF Frequency	415 kHz
RMF Amplitude	2 kA
Pulse Rate	155 Hz
Pulse Duration	125 us
Peak DC B-Field	180 G
Cathode Flow	15 sccm Xe (1.3 mg/s)
Injector Flow Xe	30 sccm Xe (2.7 mg/s)
Injector Flow CO_2	90 sccm CO_2 (2.7 mg/s)

Under a Maxwellian assumption for the plasma, these measurements yield expressions for electron temperature and density, written as:

$$1/2 = \frac{1 - \exp(-V_{d2}/T_e)}{1 - \exp(-V_{d3}/T_e)}, \tag{1}$$

$$n_e = \frac{I}{Se}\sqrt{\frac{m_i}{eT_e}}\frac{\exp(1/2)}{\exp(V_{d2}/T_e) - 1}, \tag{2}$$

where, Eq. 1 is an implicit relationship between the electron temperature T_e, the measured voltage V_{d2}, and the applied voltage V_{d3}, and Eq. 2 is an expression for the electron density as a function of the measured current I, the electrode area S, elementary charge e, and ion mass m_i. Further details on the operation of TLPs can be found in Ref. [22]. These probes are a planar type oriented with their collection face aligned with thruster wall which allows us to avoid ion ram current as well as keep the perturbations to the plasma small. The TLPs have an electrode collection area of 2 mm^2 (0.79 mm radius) with an inter-electrode spacing of 1.4 mm. These dimensions where selected such that they are both larger than the anticipated Debye length which allows us to neglect sheath expansion and assume no electrode cross-talk. We show in Fig. 2 a close up photograph of these probe assemblies as well as a photo of their locations in the thruster. In this work, we only record measurements from the center TLP because we are comparing them to the global model and seek properties that represent the bulk of the plasma. This probe is located 14.5 cm upstream from the thruster exit. We measure probe voltage with a 50:1 active differential probe, and the probe current with a 10:1 inductive Pearson coil. These measurements are then recorded with a 16 Bit digital oscilloscope at 5e6 samples/s.

IV. Model Description

The simulation tool used in this work is a 0D global plasma chemistry and kinetics code GLOBAL_KIN [23]. This software has been used extensively by the Computational Plasma Science and Engineering Group (CPSEG) at the University of Michigan to model chemically complex low temperature plasmas as well as their interaction with liquids and reactive surfaces [24, 25]. In short, GLOBAL_KIN models the plasma as a uniform body wherein the differential equations for the densities of the reactant species as well as the electron temperature are solved for given user defined reactions. The rates for electron impact reactions are calculated either though a lookup table for Maxwellian electrons or by solving Boltzmann's equation for the electron energy distribution. The details of the operation of GLOBAL_KIN can be found in Ref. [23].

We present in the appendix Tables 2 and 3, which list the reactions considered for our 2 test cases of Xe and Xe + CO_2 respectively. We in turn formulate the parameters for the model assuming a cylinder with a radius of 6 cm and a length of 32 cm which is a approximation for the conical geometry of the PEPL RMFv2 thruster. We allow for particles to flow into the volume as neutral gas and leave as a fraction of the ions thermally diffusing to the walls. In this scenario we allow for 22% of the ions to be consumed (exit the thruster) as that is the fractional surface area of the thruster exit plane and we consider these the contribution to thrust. We run the model through 10 cycles to establish quasi-steady behavior initially with a neutral gas pressure of 1.2 mTorr (Xe)/ 3.2 mTorr (CO_2) at 300 K, an electron temperature of 6.5 eV, and quasi-neutral electron density of 4×10^{10} cm^{-3}.

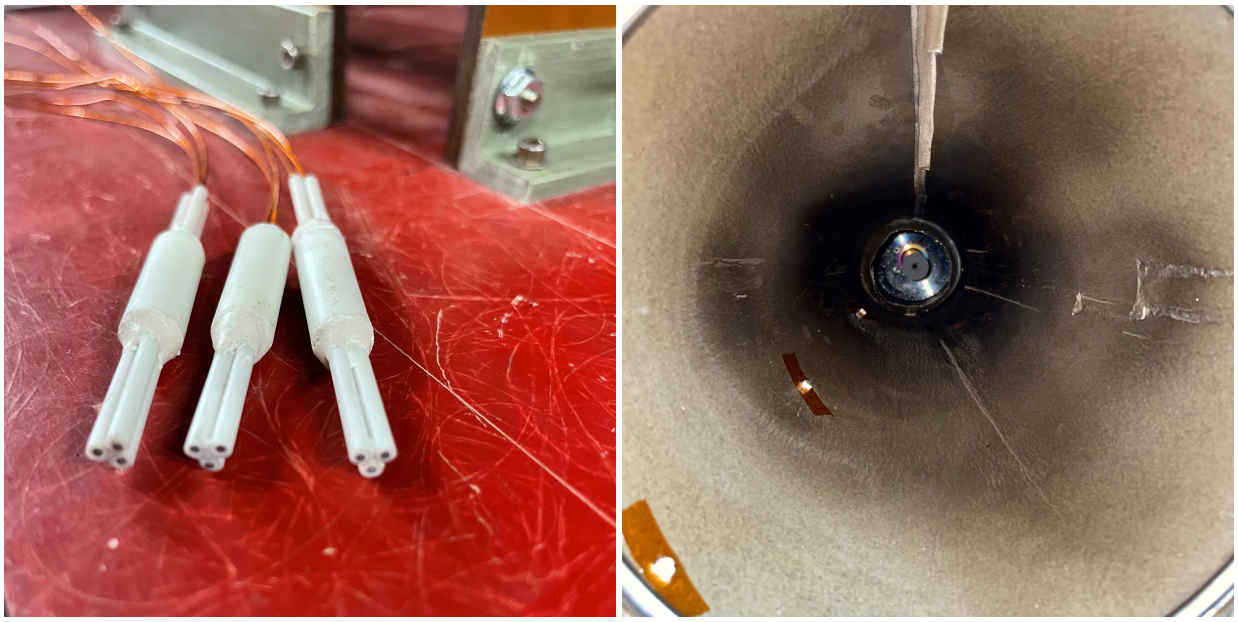

(a) (b)

Fig. 2 (a) Photograph of wall triple Langmuir probes. (b) Photo of TLPs installed along the wall of the RMF thruster

We model power deposition to the electrons as a pre-prescribed function that is synthesized from the envelope of the RMF antenna currents in vacuum and the product of turn-on and turn-off sigmoid functions to stand in for the effect of electron density on power absorption. We show these functions and their normalized product in Fig. 3. The magnitude of the power deposition in the model is tuned to match the coupled energy into the plasma as calculated from the attenuation of RMF antenna currents following the procedure by Gill et al. [19]. Note, we set the cycle time for these cases to 6.5 ms in accordance with the 155 Hz pulse repetition rate used in the experimental work. For the Xe case the coupled energy was set to 6.4 J for the RMF, and for the CO_2 case the energy was set to 0.6 J. In both cases, we provide a background 400W constant 'cathode' discharge which is commensurate with the experiment. This brings the total energy for the Xe case to 9.0 J and 3.2 J for the CO_2 case.

To compare loss mechanisms of interest we track both the rate of production of excited states as well as the rate of dissociation and rotational and vibrations excitation of the relevant species. The total energy loss due to a given species is calculated by accounting for its production using the following equation:

$$E_{loss,i} = V\epsilon_i \int_0^\tau \sum_j \left(a_{ij} k_j \prod_r n_{rj}^{a_{rj}} \right) dt, \tag{3}$$

where V is the volume of the thruster, τ is the cycle time, ϵ_i is the enthaply of formation of product i, a_{ij} is the stoichiometric coefficient of species i in reaction j, k_j is the rate of reaction j, and n_r is the density of reactants. Furthermore, we account for the power loss of electrons to the walls with the following equation:

$$P_{diffusion} = A\frac{1}{4} n_e \sqrt{\frac{8eT_e}{\pi m_e}} \left(2eT_e + e\phi\right) \exp\left(-\frac{\phi}{T_e}\right), \tag{4}$$

where A is the total surface area (22% of power counted as thrust), n_e is the plasma density, T_e is the electron temperature in eV, m_e is the electron mass, and ϕ is the potential drop across the sheath which we will define as

$$\phi = T_e \ln\left(\sqrt{\frac{m_i}{2\pi m_e}}\right). \tag{5}$$

As a point of comparison, we can form an effective plasma efficiency from the results of the model. For the overall thruster, the plasma efficiency is defined as the ratio of the thermal and magnetic energy in the plasma to the total energy

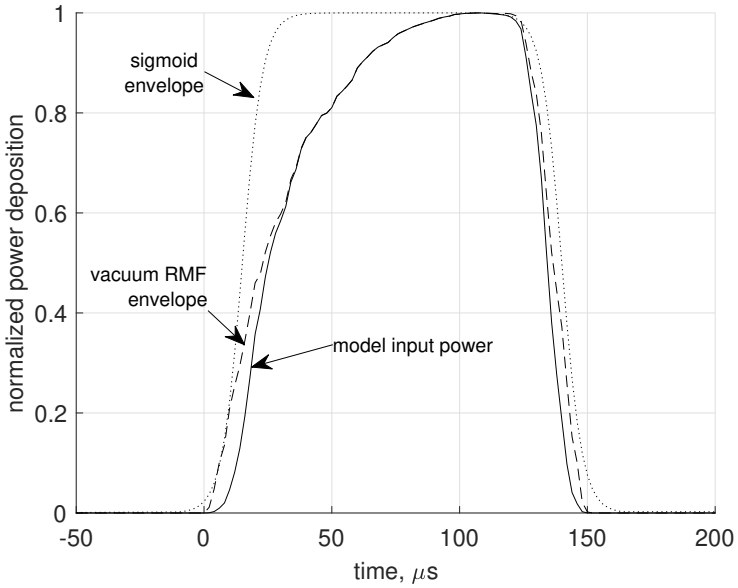

Fig. 3 Normalized RMF current envelope in vacuum, product of turn-on and turn-off sigmoid functions, and resultant power deposition curve used in the model.

coupled to the plasma [19]. Here, we will co-opt this framework and define our plasma efficiency as

$$\eta_p = \frac{\int_0^\tau P_{thrust}\, dt}{E_p}, \tag{6}$$

where $P_{thrust} = 0.22 P_{diffusion}$ is the power to thrust, and E_p is the total energy coupled into the plasma.

V. Results

In this section, we present the results for our two propellant cases which we numerically modeled. We compare the simulated Xe and CO_2 cases to the experimentally determined plasma temperature and density measurements from the TLPs embedded inside the thruster wall.

A. Xenon case

We show in Figs. 4 and 5 the results of the xenon case model and experimental measurements. Starting in Fig. 4a we show the electron (plasma) density from the model and experiment as well as the neutral xenon density from the model. We note that the model and experimental results for electron density are not in good agreement; however, their general shape is faithfully reproduced. Notably, the peak in ionization for the experiment is on the order of 3 times what it is for the model, reaching up to 4×10^{13} cm^{-3} as opposed to the model's peak at 1.4×10^{13} cm^{-3}. Additionally, the onset of ionization in the experiment lags behind the model by roughly 50 μs. This is likely a result of the imposed power deposition in the model as it is not a function of existing electron density which could induce this delay. Looking now at Fig. 4b we show the electron temperature from the model and the experiment where there is generally poor agreement. However, the trends generally still hold with an early rise in temperature followed by cooling as the plasma rarefies and a brief heating point as the excited states de-excite and transfer some energy back to the electrons. There are issues with how the model calculates electron temperature as shown here. When the plasma density is lost to recombination and diffusion ($t = 75\mu$s), the model is still enforcing power deposition into the electrons, and therefore the electron temperature increases to effectively infinity in the time between 75 and 125 μs. Because this is a non-physical effect, we have not shown the top of the electron temperature for the model here and this region should be disregarded.

Moving on to Fig. 5, we show the energy losses for the product species in Fig. 5a in addition to the energy contributions of diffusion and thrust. The thrust and diffusion energies sum to the remainder of the input energy, and we

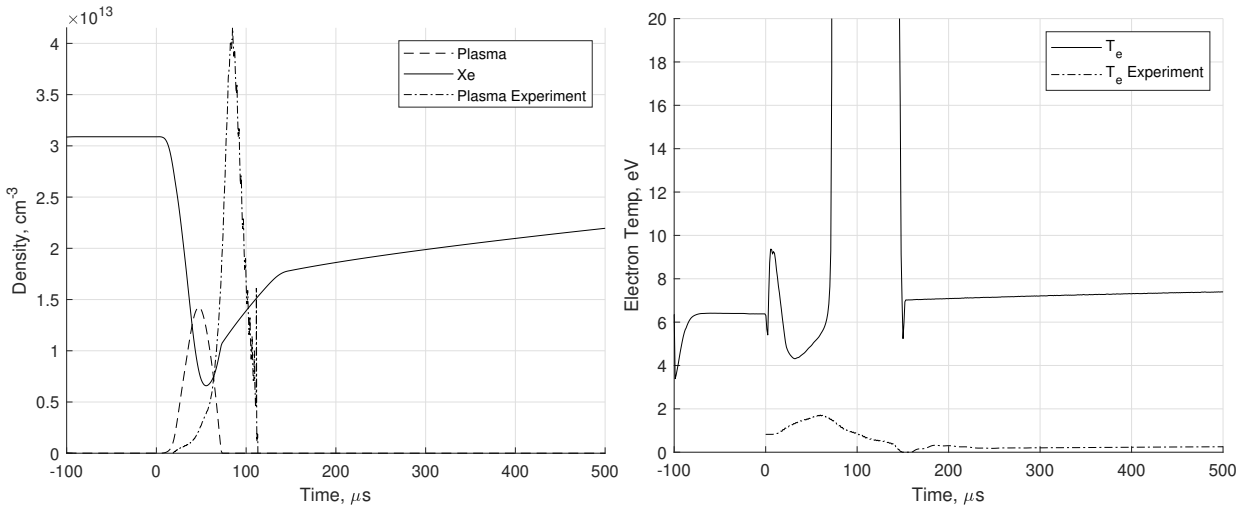

Fig. 4 Xenon model results compared to experiment (a) electron and neutral density (b) electron temperature.

assign 22% of this total diffusion energy as thrust energy as we discussed in section IV. We can calculate an effective plasma efficiency for the simulation by taking the ratio of the thrust energy to the input energy (9.0 J for xenon). In this case, the efficiency estimate is 3.8% — not surprising given we only assume thrust is thermal — which is close to what we would expect for the plasma efficiency of a similar operating condition (10.9%) [19]. Notably, the percentage of the total energy caused by collisions (from 'E' bar in Fig. 5a) is 84% and the percentage of the energy caused by wall diffusion is 14%. The difference between these two modes agrees well with prior experimental measurements for these loss channels [26].

In Fig. 5b we show the energy loss for the significant (> 0.1 J) reactions. We note that the top three loss-producing reactions in this case in order are the production of the 9.45 eV xenon excited state from the ground state (E + XE → XE** + E), xenon ionization (E + XE → XE+ + E + E), and the production of the 9.45 eV xenon excited state from the 8.32 eV excited state (E + XE* → XE** + E). Interestingly, the production of Xe** dominates over the loss caused by the production of the 8.32 eV which is typically considered the primary excitation source in xenon [27].

B. Carbon dioxide case

Turning now to the results for the CO_2 case, we show in Figs. 6 and 7 the results of the model compared to our experiment. Again, we can note in Fig. 6a that the model underpredicts the experimental level of ionization by a factor of roughly 3 in addition to the peak ionization in the model occurring approximately 50 μs ahead of the experiment. We can also see in the figure that due to the low input energy from the RMF (only 0.6 J), a significant amount of the propellant remains unionized during the pulse. This indicates a low mass utilization, which is to be expected given the higher effective ionization energy of the gas mixture. In, Fig. 6b we see that similar to the xenon case, the experimental values of electron temperature have poor agreement with the model results. Again, we see for the experiment that the electron temperature spikes after the electron density drops to zero; however, this is not seen in the model because the low ionization does not lead to as rapid of a decline in electron density. Interestingly, the experimental electron temperature exhibits a low-frequency oscillation on the order of 40 kHz in the afterglow period. This effect is seemingly too low frequency to be caused by the 415 kHz RMF but could be caused by ringing in the measurement circuit or some oscillating reaction mechanism not included in the model.

We show in Fig. 7 the energy breakdown for carbon dioxide. In this case, the efficiency estimate is 9.2% which is close to a 2.5x improvement over the xenon case. However, given that the energy coupled for the CO_2 is so little one would expect that the overall efficiency for the system would be insignificantly close to zero. From Fig. 7a, we see that the lossiest species include the production and ionization of atomic and molecular oxygen, carbon monoxide, and again the ionization and excitation of xenon. We show in Fig. 7b that the primary loss reactions in order are electron impact dissociation of carbon dioxide (E + CO2 → CO + O + E), ionization of oxygen (E + O → O+ + E + E), and the ionization of carbon monoxide (E + CO → CO+ + E + E).

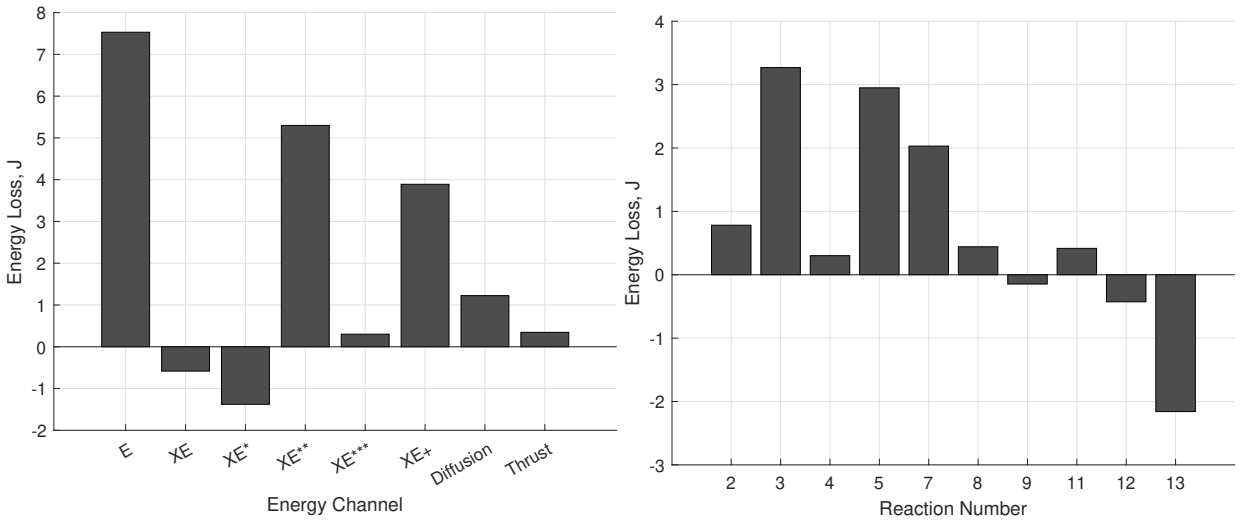

(a) **(b)**

Fig. 5 Xenon model energetic losses (a) energy loss from plasma from different channels as well as energy consumed by diffusion and thrust (b) collisional energy loss in significant (>0.1 J) reactions. Negative energies correspond to energy gain to the electrons from de-excitation. Reaction numbers are listed in Table 2

.

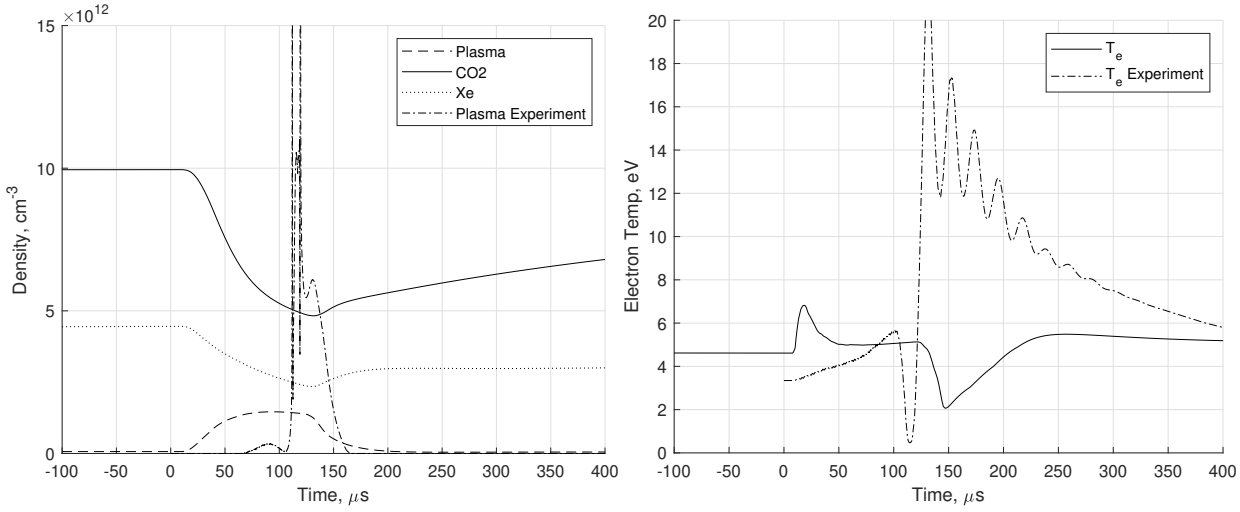

(a) **(b)**

Fig. 6 CO_2 model results compared to experiment (a) electron and neutral density (b) electron temperature

VI. Discussion

In this section, we begin with a discussion of the sources of error and caveats with the experimental measurements and model. Following this, we present suggestions on how to improve RMF thruster performance given the results of this work.

A. Experiment and Model Considerations

The use of the TLPs in this experiment is necessitated by the speed required to resolve the RMF pulse, however, their measurements assume a Maxwellian, non-flowing, and demagnetized plasma. We likely do not meet those criteria in our experiment and we have taken steps to mitigate the error, such as using a planar style probe oriented along the wall. However, systematic error due to these effects is difficult to quantify due to our limited information. We estimate it

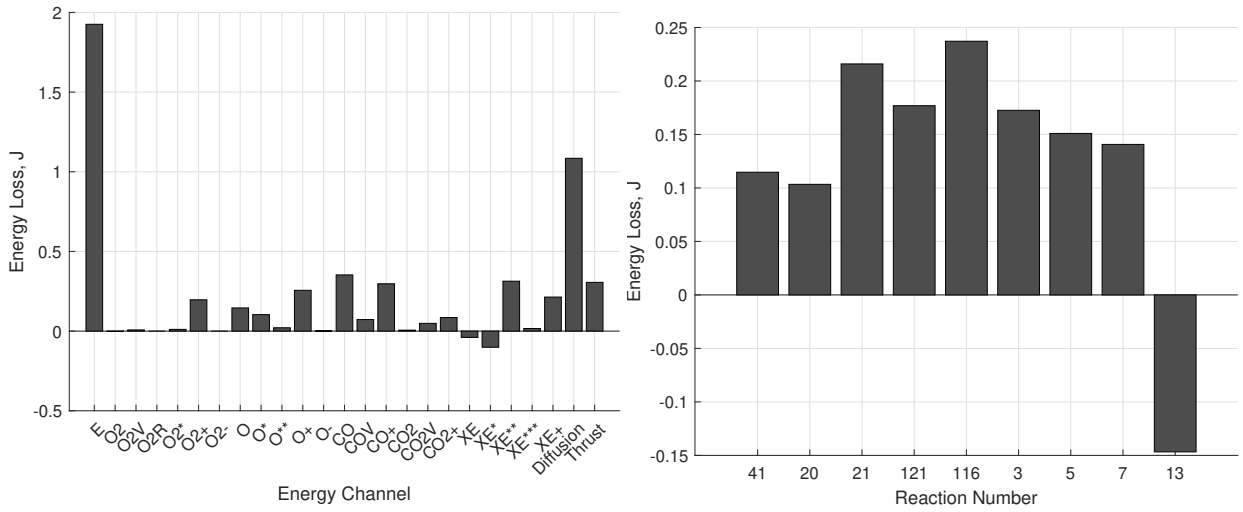

(a) **(b)**

Fig. 7 CO_2 model energetic losses (a) energy loss from plasma from different channels as well as energy consumed by diffusion and thrust (b) collisional energy loss in significant (>0.1 J) reactions. Negative energies correspond to energy gain to the electrons from de-excitation. Reaction numbers are listed in Table 3.

is likely around 20-30% of the reported values based on analysis of Langmuir probes used in other EP devices [28]. Furthermore, the TLP requires a user-set bias voltage which should be on the order of the electron temperature. This is problematic as we require a priori knowledge of the electron temperature. We have selected a bias voltage that was acceptably in the range of our anticipated electron temperatures, however, the effect of bias voltage on our measurements has not been carefully evaluated and also will contribute to the error in the measurements. Lastly for the probes, as mentioned in section III we take our experimental values for the plasma parameters from the center plasma TLP as it is best located to measure the global plasma parameters. However, it is still located along the wall and therefore is not necessarily an adequate representative of the bulk plasma. A trade-off had to be made for this work between access and perturbation effects, as the wall probe does not affect the plasma as significantly as an injected probe.

The major caveat to the modeling work presented here is the enforced power deposition curve from Fig. 3. While this plot is based on some of our physical understanding of the RMF thruster, ultimately the power absorption of plasma is strongly dependent on the present electron density as is the case for most discharges. Since we enforce the deposition in our model, we end up with artifacts of that decision such as the extreme electron temperature in Fig. 4b and the early onset of ionization in Figs. 4a and 6a. Unfortunately, how the RMF couples energy into the plasma is a unique and poorly understood process, and efforts to model it remain an active area of research. However, lumped circuit models for inductive thrusters have been used successfully in the past to match circuit waveforms for both RMF and other technologies [29, 30]. Pairing these types of models with a global chemistry model could provide good closure for both the energy deposition into the chemical reactions and the effective plasma resistance in the circuit model.

B. Impacts for Thruster Design

From our model results, we see that the change in propellant from pure xenon to a xenon CO_2 mixture did not indicate a significant boost in thruster performance. The very low ionization in the CO_2 case points to a very poor overall efficiency. However, the low density did allow us to prove that a reduction in density does result in a reduction of the radiation losses as well as an increase in the effective plasma efficiency. In our model, a reduction in density by roughly 10x between the cases resulted in a 3x increase in plasma efficiency as well as an expected decrease in the ratio of collision loss to wall diffusion losses.

Our selection of CO_2 as a propellant, however, proved to be a poor choice. As the dissociation of CO_2 into CO and O form electron impact is prevalent and lossy. From these results, we conjecture that an ideal candidate for an inductive thruster alternative propellant is both chemically and electrically inactive. Xenon, while being inert and easily ionized has many electrons in high orbitals to excite, and CO_2 is easily capable of reacting with itself to lose energy. A propellant like H2 may be a suitable candidate for inductive thrusters as it can no longer be electrically excited once

ionized. Alternatively, a choice like N2 or NH3 may be good, as N2 has few reactions other than dissociation, and the conversion of NH3 to H2 and N2 is very energetically unfavorable. We aim to assess these and other propellants using the framework we present here to both prove the performance of inductive thrusters on alternative propellants as well as improve their performance.

VII. Conclusion

In this work, we sought to evaluate the performance of an inductive pulsed plasma thruster, namely a rotating magnetic field thruster on various propellants. To this end, we performed experimental measurements of the interior plasma properties of the thruster and compared them to a global plasma chemistry model with Maxwellian electrons. We performed two studies, one using pure xenon at a flow rate of 45 sccm (4.0 mg/s) and another using a xenon CO_2 mix at a combined flow rate of 105 sccm (4.0 mg/s). We found that the xenon case exhibited large collisional losses primarily from the production of Xe** (9.45 eV) and Xe+ (12.13 eV) and had an effective plasma efficiency of 3.8%. Furthermore, we found that the CO_2 case had very little ionization and energy coupling. Electron energy in this case was primarily lost due to the production of CO, O, O+, and CO+, however, the decrease in plasma density did allow for an increase in plasma efficiency up to 9.2%. We discussed the major limitations of this work, including the imposed profile of energy deposition, and proposed pairing the chemical model to a lump circuit model for improved fidelity. We concluded by suggesting several additional alternative propellants for the RMF thruster, which are the subject of future evaluation.

Acknowledgments

We would like to thank Eagle Harbor Technologies for their development of the RMF power processing unit and their technical support, as well as Dr. Mark Kushner and Dr. Mackenzie Meyer from the Computational Plasma Science and Engineering Group at the University of Michigan for the use of GLOBAL_KIN and their assistance. Furthermore, we would like acknowledge NASA for funding this work through NSTGRO Fellowship grant Number 80NSSC20K1168, and NSTRF Fellowship grant number 80NSSC18K1190, as well as the AFOSR Space Propulsion and Power program.

Appendix

Table 3 Table of reactions for CO_2

Number	Reaction
1	E + XE → XE + E
2	E + XE → XE* + E
3	E + XE → XE** + E
4	E + XE → XE*** + E
5	E + XE → XE^+ + E + E
6	E + XE* → XE* + E
7	E + XE* → XE** + E
8	E + XE* → XE^+ + E + E
9	E + XE* → XE + E
10	E + XE** → XE** + E
11	E + XE** → XE^+ + E + E
12	E + XE** → XE + E
13	E + XE** → XE* + E
14	E + XE*** → XE*** + E
15	E + XE*** → XE^+ + E + E
16	E + XE*** → XE + E
17	E + XE^+ → XE^+ + E

Table 3 Table of reactions for CO_2

Number	Reaction
18	E + XE^+ → XE
19	E + O → O + E
20	E + O → O* + E
21	E + O → O^+ + E + E
22	E + O + O2 → O- + O2
23	E + O* → O* + E
24	E + O* → O + E
25	E + O* → O^+ + E + E
26	E + O^+ → E + O^+
27	E + E + O^+ → O + E
28	E + O2 + O^+ → O + O2
29	E + CO2 + O^+ → O + CO2
30	E + O- → O- + E
31	E + O- → O + E + E
32	E + O2 → O2 + E
33	E + O2 → O2R + E
34	E + O2 → O2V + E
35	E + O2 → O2V + E
36	E + O2 → O2V + E
37	E + O2 → O2V + E
38	E + O2 → O2V + E
39	E + O2 → O2V + E
40	E + O2 → O2* + E
41	E + O2 → $O2^+$ + E + E
42	E + O2 → O + O + E
43	E + O2 → O + O + E
44	E + O2 → O^+ + O + E + E
45	E + O2 → O- + O
46	E + O2 + O2 → O2- + O2
47	E + O2V → O2V + E
48	E + O2V → O- + O
49	E + O2V → O2R + E
50	E + O2V → O2 + E
51	E + O2V → O2* + E
52	E + O2V → O + O + E
53	E + O2V → O + O + E
54	E + O2V → $O2^+$ + E + E
55	E + O2V → O^+ + O + E + E
56	E + O2* → O2* + E
57	E + O2* → O + O + E
58	E + O2* → O + O + E
59	E + O2* → O^+ + O + E + E

Table 3 Table of reactions for CO_2

Number	Reaction
60	E + O2* → O- + O
61	E + O2* → O2 + E
62	E + O2* → $O2^+$ + E + E
63	E + O2* + O2 → O2- + O2
64	E + $O2^+$ → E + $O2^+$
65	E + $O2^+$ → O + O
66	E + E + $O2^+$ → O2 + E
67	E + O2 + $O2^+$ → O2 + O2
68	E + CO2 + $O2^+$ → O2 + CO2
69	E + O2- → O2- + E
70	E + O2- → O2 + E + E
71	O + O + O2 → O2 + O2
72	O + O + O2 → O2* + O2
73	O + O + CO2 → O2* + CO2
74	O + O* + O2 → O2 + O2
75	O + O* + CO2 → O2 + CO2
76	O + O^+ + CO2 → $O2^+$ + CO2
77	O + O- → O2 + E
78	O + O2- → O2 + O-
79	O* + O2 → O2* + O
80	O* + $O2^+$ → O2* + O^+
81	O* + O2 → O2 + O
82	O* + CO2 → CO2 + O
83	O^+ + O- → O + O
84	O^+ + O2 → O + $O2^+$
85	O^+ + O2* → O + $O2^+$
86	O^+ + O2- → O + O2
87	O^+ + O2- → O + O + O
88	O- + O2 → O2- + O
89	O- + O2* → O2- + O
90	O- + $O2^+$ → O + O2
91	O- + $O2^+$ → O + O + O
92	O2V + O2 → O2 + O2
93	O2R + O2 → O2 + O2
94	O2* + O2* → O2 + O2
95	O2* + O2- → O2 + O2 + E
96	O2* + O2 → O2 + O2
97	O2* + O → O2 + O
98	$O2^+$ + O2- → O2 + O2
99	$O2^+$ + O2- → O2 + O + O
100	$O2^+$ + O2- → O + O + O + O
101	$O2^+$ + O2- + O2 → O2 + O2 + O2

Table 3 Table of reactions for CO_2

Number	Reaction
102	$O2^+ + O2^- + CO2 \rightarrow O2 + O2 + CO2$
103	$O2^- + O2 \rightarrow O2 + E + O2$
104	$O2^- + CO2 \rightarrow O2 + E + CO2$
105	$O2^* \rightarrow O2$
106	$E + CO2 \rightarrow CO2V + E$
107	$E + CO2 \rightarrow CO2V + E$
108	$E + CO2 \rightarrow CO2V + E$
109	$E + CO2 \rightarrow CO2V + E$
110	$E + CO2 \rightarrow CO2V + E$
111	$E + CO2 \rightarrow CO2V + E$
112	$E + CO2 \rightarrow CO2V + E$
113	$E + CO2 \rightarrow CO2V + E$
114	$E + CO2 \rightarrow CO + O^-$
115	$E + CO2 \rightarrow CO + O + E$
116	$E + CO2 \rightarrow CO + O + E$
117	$E + CO2 \rightarrow CO2^+ + E + E$
118	$E + CO2V \rightarrow CO2 + E$
119	$E + CO2^+ \rightarrow CO + O$
120	$E + CO \rightarrow COV + E$
121	$E + CO \rightarrow CO^+ + E + E$
122	$E + CO \rightarrow CO^+ + E + E$
123	$E + CO \rightarrow CO^+ + E + E$
124	$E + CO \rightarrow CO^+ + E + E$
125	$E + CO \rightarrow CO^+ + E + E$
126	$E + COV \rightarrow CO + E$
127	$O^+ + CO2 \rightarrow CO2^+ + O$
128	$CO2^+ + O2 \rightarrow O2^+ + CO2$
129	$CO2^+ + O \rightarrow O^+ + CO2$
130	$CO2^+ + O \rightarrow O2^+ + CO$
131	$CO2^+ + CO \rightarrow CO2 + CO^+$
132	$CO^+ + CO2 \rightarrow CO2^+ + CO$
133	$CO^+ + O2 \rightarrow O2^+ + CO$
134	$CO^+ + O \rightarrow O^+ + CO$
135	$O^- + CO \rightarrow CO2 + E$
136	$CO2^+ + O2^- \rightarrow CO2 + O2$
137	$CO^+ + O2^- \rightarrow CO + O2$
138	$CO2 + O \rightarrow CO + O2$
139	$CO + O2 \rightarrow CO2 + O$
140	$CO + O + O2 \rightarrow CO2 + O2$
141	$CO + O + CO2 \rightarrow CO2 + CO2$
142	$O^- + CO2^+ \rightarrow O + CO2$
143	$O^- + CO^+ \rightarrow O + CO$

Table 3 Table of reactions for CO_2

Number	Reaction
144	CO2 + O2 → CO + O + O2
145	CO2 + CO2 → CO + O + CO2
146	O* + CO → CO2
147	O* + CO → CO + O
148	O* + CO2 → O2 + CO
149	CO2V + O2 → CO2 + O2
150	CO2V + CO2 → CO2 + CO2
151	CO2 + O2 → CO2V + O2
152	CO2 + CO2 → CO2V + CO2
153	COV + O2 → CO + O2
154	COV + CO2 → CO + CO2
155	CO + O2 → COV + O2
156	CO + CO2 → COV + CO2
157	O** → O^+ + E
158	O2 → $O2^+$ + E
159	O** → O
160	E + O → O** + E
161	E + O** → O** + E
162	E + O** → O + E
163	E + O** → O^+ + E + E
164	O** + O2 → O + O2*
165	O** + O2 → O + O2
166	O** + CO2 → O + CO2

References

[1] Braun, R., Myers, R., and Bragg-Sitton, S., "Space nuclear propulsion for human mars exploration," *NASEM Space Nuclear Propulsion Technologies Committee Report. Washington, DC: National Academies of Sciences, Engineering and Medicine*, 2021.

[2] Polzin, K. A., "Scaling and systems considerations in pulsed inductive plasma thrusters," *IEEE Transactions on Plasma Science*, Vol. 36, 2008, pp. 2189–2198. https://doi.org/10.1109/TPS.2008.2003537.

[3] Polzin, K., Martin, A., Little, J., Promislow, C., Jorns, B., and Woods, J., "State-of-the-art and advancement paths for inductive pulsed plasma thrusters," *Aerospace*, Vol. 7, 2020, pp. 1–67. https://doi.org/10.3390/AEROSPACE7080105.

[4] Rovey, J. L., Lyne, C. T., Mundahl, A. J., Rasmont, N., Glascock, M. S., Wainwright, M. J., and Berg, S. P., "Review of multimode space propulsion," *Progress in Aerospace Sciences*, Vol. 118, 2020, p. 100627. https://doi.org/10.1016/j.paerosci.2020.100627, URL https://doi.org/10.1016/j.paerosci.2020.100627.

[5] Polzin, K. A., Martin, A. K., Eskridge, R. H., Kimberlin, A. C., Addona, B. M., Devineni, A. P., Dugal-Whitehead, N. R., and Hallock, A. K., "Summary of the 2012 Inductive Pulsed Plasma Thruster Development and Testing Program," , 2013. URL https://ntrs.nasa.gov/api/citations/20140002426/downloads/20140002426.pdf.

[6] Mikellides, P. G., "Pulsed Inductive Thruster (PIT): Modeling and Validation Using the MACH2 Code," , 2003. URL http://hdl.handle.net/2060/20040027584.

[7] Kirtley, D. E., Slough, J. T., Pfaff, M., and Pihl, C., "Steady Operation of an Electromagnetic Plasmoid Thruster," , 2011.

Table 2 Table of reactions for Xe

Number	Reaction
1	$E + XE \rightarrow XE + E$
2	$E + XE \rightarrow XE^* + E$
3	$E + XE \rightarrow XE^{**} + E$
4	$E + XE \rightarrow XE^{***} + E$
5	$E + XE \rightarrow XE^+ + E + E$
6	$E + XE^* \rightarrow XE^* + E$
7	$E + XE^* \rightarrow XE^{**} + E$
8	$E + XE^* \rightarrow XE^+ + E + E$
9	$E + XE^* \rightarrow XE + E$
10	$E + XE^{**} \rightarrow XE^{**} + E$
11	$E + XE^{**} \rightarrow XE+ + E + E$
12	$E + XE^{**} \rightarrow XE + E$
13	$E + XE^{**} \rightarrow XE^* + E$
14	$E + XE^{***} \rightarrow XE^{***} + E$
15	$E + XE^{***} \rightarrow XE^+ + E + E$
16	$E + XE^{***} \rightarrow XE + E$
17	$E + XE^+ \rightarrow XE^+ + E$
18	$E + XE^+ \rightarrow XE$

[8] Waldock, J., Kirtley, D. E., and Slough, J. T., "Electromagnetic Optimization of FRC-Based Pulsed Plasma Thrusters," 2013, pp. 1–14.

[9] Sercel, C. L., Gill, T., Woods, J. M., and Jorns, B., "Performance Measurements of a 5 kW-Class Rotating Magnetic Field Thruster," American Institute of Aeronautics and Astronautics, 2021, pp. 1–26. https://doi.org/10.2514/6.2021-3384, URL https://arc.aiaa.org/doi/10.2514/6.2021-3384.

[10] Mikellides, P. G., and Villarreal, J. K., "High energy pulsed inductive thruster modeling operating with ammonia propellant," *Journal of Applied Physics*, Vol. 102, 2007, pp. 1–12. https://doi.org/10.1063/1.2809436.

[11] Polzin, K. A., "Comprehensive review of planar pulsed inductive plasma thruster research and technology," *Journal of Propulsion and Power*, Vol. 27, 2011, pp. 513–531. https://doi.org/10.2514/1.B34188, URL http://arc.aiaa.org/doi/10.2514/1.B34188.

[12] Slough, J. T., Kirtley, D. E., and Weber, T. E., "Pulsed Plasmoid Propulsion: The ELF Thruster," 2009, pp. 1–24. URL https://s3-us-west-2.amazonaws.com/pnwmsnw/ELF_IEPC-2009-265.pdf.

[13] Weber, T. E., Slough, J. T., and Kirtley, D. E., "The electrodeless Lorentz force (ELF) thruster experimental facility," *Review of Scientific Instruments*, Vol. 83, 2012, pp. 83,113509. https://doi.org/10.1063/1.4759000.

[14] Furukawa, T., Shimura, K., Kuwahara, D., and Shinohara, S., "Verification of azimuthal current generation employing a rotating magnetic field plasma acceleration method in an open magnetic field configuration," *Physics of Plasmas*, Vol. 26, 2019. https://doi.org/10.1063/1.5064392, URL http://dx.doi.org/10.1063/1.5064392.

[15] Furukawa, T., Shinohara, S., and Kuwahara, D., "Electrodeless plasma propulsion with electromagnetic acceleration effect by using rotating magnetic field current drive method," *AIAA Propulsion and Energy 2020 Forum*, 2020, pp. 1–11. https://doi.org/10.2514/6.2020-3630.

[16] Woods, J. M., Sercel, C. L., Gill, T. M., and Jorns, B. A., "Performance measurements of a rotating magnetic field thruster," *AIAA Propulsion and Energy 2020 Forum*, Vol. 3633, 2020, pp. 1–18. https://doi.org/10.2514/6.2020-3633.

[17] Sercel, C. L., Woods, J. M., Gill, T. M., and Jorns, B. A., "Impact of flux conservers on performance of inductively driven pulsed plasmoid thrusters," *AIAA Propulsion and Energy 2020 Forum*, 2020, pp. 1–17. https://doi.org/10.2514/6.2020-3632.

[18] Weber, T., "The Electrodeless Lorentz Force Thruster Experiment," , 2010. URL https://digital.lib.washington.edu/researchworks/handle/1773/20069.

[19] Gill, T., Sercel, C. L., Woods, J. M., and Jorns, B. A., "Experimental Characterization of Efficiency Modes in a Rotating Magnetic Field Thruster," American Institute of Aeronautics and Astronautics, 2022. https://doi.org/10.2514/6.2022-2191, URL https://arc.aiaa.org/doi/10.2514/6.2022-2191.

[20] Miller, K. E., Prager, J., Henson, A., McEleney, K., Woods, J., Sercel, C., Gill, T., Viges, E., and Jorns, B., "Continuously-Operating Repetitively-Pulsed RMF-FRC Thruster and Power System," *2021 IEEE International Conference on Plasma Science (ICOPS)*, 2021, pp. 1–1. https://doi.org/10.1109/ICOPS36761.2021.9588361.

[21] Dankanich, J. W., Walker, M. L. R., Swiatek, M. W., and Yim, J. T., "Recommended practice for pressure measurement and calculation of effective pumping speed in electric propulsion testing," *Journal of Propulsion and Power*, Vol. 33, 2017, pp. 668–680. https://doi.org/10.2514/1.B35478.

[22] Chen, S. L., and Sekiguchi, T., "Instantaneous direct-display system of plasma parameters by means of triple probe," *Journal of Applied Physics*, Vol. 36, 1965, pp. 2363–2375. https://doi.org/10.1063/1.1714492.

[23] Dorai, R., "Modeling of atmospheric pressure plasma processing of gases and surfaces," , 2002.

[24] Huang, S., Volynets, V., Hamilton, J. R., Lee, S., Song, I.-C., Lu, S., Tennyson, J., and Kushner, M. J., "Insights to scaling remote plasma sources sustained in NF3 mixtures," *Journal of Vacuum Science & Technology A: Vacuum, Surfaces, and Films*, Vol. 35, No. 3, 2017, p. 031302.

[25] Bhoj, A. N., and Kushner, M. J., "Avalanche process in an idealized lamp: II. Modelling of breakdown in Ar/Xe electric discharges," *Journal of Physics D: Applied Physics*, Vol. 37, No. 18, 2004, p. 2510.

[26] Gill, T. M., Sercel, C. L., and Jorns, B. A., "Experimental Investigation into Mechanisms for Energy Loss in a Rotating Magnetic Field Thruster," , 2022.

[27] Hayashi, M., "Luminous layers in the prebreakdown region of low pressure noble gases," , 1982.

[28] Lobbia, R. B., and Beal, B. E., "Recommended practice for use of langmuir probes in electric propulsion testing," *Journal of Propulsion and Power*, Vol. 33, 2017, pp. 566–581. https://doi.org/10.2514/1.B35531.

[29] Woods, J. M., Sercel, C. L., Gill, T., and Jorns, B., "Equivalent Circuit Model for a Rotating Magnetic Field Thruster," *AIAA Propulsion and Energy 2021 Forum*, 2021, p. 3400.

[30] Polzin, K. A., Hallock, A. K., Sankaran, K., and Little, J. M., *Circuit Modeling of Inductively-Coupled Pulsed Accelerators*, CRC Press, 2022.